



# In situ multiplexed imaging of miRNA heterogeneity in single urinary exosome enables non-invasive bladder cancer diagnosis

Yang Wang<sup>a,1</sup>, Huaxing Li<sup>a,1</sup>, Xiangqian Cao<sup>a,1</sup>, Weiguang Zhao<sup>b</sup>, Hongquan Gou<sup>c</sup>, Chenkai Yang<sup>b</sup>, Haoyuan Wang<sup>b</sup>, Jie Deng<sup>c</sup>, Wen Chen<sup>c</sup>, Haipeng Qi<sup>c</sup>, Dongsheng Mao<sup>c,\*</sup>, Xiaoli Zhu<sup>c,\*</sup>, Bing Shen<sup>a,b,d,\*\*</sup>

<sup>a</sup> Department of Urology, Shanghai General Hospital, Shanghai Jiao Tong University School of Medicine, Shanghai, 200080, China

<sup>b</sup> Department of Urology, Shanghai Tenth People's Hospital, School of Medicine, Tongji University, Shanghai, 200072, China

<sup>c</sup> Department of Clinical Laboratory Medicine, Shanghai Tenth People's Hospital, School of Medicine, Tongji University, Shanghai, 200072, China

<sup>d</sup> Urologic Cancer Institute, School of Medicine, Tongji University, Shanghai, 200092, China

## ARTICLE INFO

### Keywords:

Urinary exosome  
Bladder cancer  
Exosomal miRNA  
Heterogeneity analysis  
Non-invasive diagnosis

## ABSTRACT

Urine-based non-invasive diagnostics provide a promising approach for the screening and recurrence monitoring of urinary tumors, including bladder cancer. Among these, the analysis of urinary exosomal contents, particularly miRNAs, holds significant diagnostic potential. However, achieving in situ multiplexed analysis of single-exosome miRNAs to uncover exosome heterogeneity and enhance tumor diagnostics remains a major challenge. Here, we address this challenge by engineering artificial vesicles based on flat framework nucleic acid to enable targeted membrane fusion with bladder cancer-derived exosomes, facilitating in situ analysis of five exosomal contents. Using this strategy, we revealed single-particle heterogeneity in urinary exosomal miRNA expression and achieved highly sensitive and specific non-invasive diagnosis of bladder cancer, with both sensitivity and specificity reaching 100 %. This study establishes an optical imaging-based paradigm for multiplexed analysis of exosomal contents, single-exosome heterogeneity assessment, and non-invasive diagnostics using urinary exosomes.

## 1. Introduction

Bladder cancer is one of the most common malignancies of the urinary system. The current gold standard for clinical diagnosis relies on cystoscopy, often combined with tissue biopsy of abnormal areas [1,2]. Patients with non-muscle invasive bladder cancer (NMIBC) require frequent cystoscopic follow-up after surgery [3,4]. However, cystoscopy is invasive, expensive, and associated with patient anxiety and other side effects, while its sensitivity for detecting early-stage bladder cancer remains limited [5,6]. In contrast, urine collection is a simple, non-invasive, and highly accessible method that provides stable samples for clinical analysis. Its non-invasive nature enables continuous disease monitoring, and urinary content analysis has already demonstrated broad clinical utility [7,8]. Notably, urinary exosomes are rich in disease biomarkers, offering a platform for comprehensive multi-analyte

profiling of tumors such as bladder cancer. Moreover, exosomes provide a protective environment for unstable biomarkers such as miRNAs, making them particularly valuable. As a result, urinary exosomes emerge as an ideal target for non-invasive diagnosis and post-surgical monitoring of bladder cancer.

Exosomes are secreted by almost all human cells, and heterogeneity analysis of exosomes from specific sources holds immense potential for the precise diagnosis of bladder cancer. miRNAs, small non-coding RNA molecules typically comprising ~22 nucleotides, primarily regulate gene expression and play crucial roles in processes such as cell proliferation and differentiation [9,10]. Recent studies have shown that miRNAs within exosomes have greater diagnostic potential than free miRNAs [11,12]. Furthermore, the combined analysis of differentially expressed miRNAs can significantly improve the specificity and sensitivity of bladder cancer diagnosis [13,14]. Current RNA quantification

\* Corresponding authors.

\*\* Correspondence to: B. Shen, Department of Urology, Shanghai Tenth People's Hospital, School of Medicine, Tongji University, Shanghai, 200072, China.

E-mail addresses: [dongsheng\\_mao@tongji.edu.cn](mailto:dongsheng_mao@tongji.edu.cn) (D. Mao), [xiaolizhu@tongji.edu.cn](mailto:xiaolizhu@tongji.edu.cn) (X. Zhu), [urodrshenbing@shsmu.edu.cn](mailto:urodrshenbing@shsmu.edu.cn) (B. Shen).

<sup>1</sup> These authors contributed equally to this work.

techniques, including reverse transcription-quantitative polymerase chain reaction (RT-qPCR) and next-generation sequencing (NGS) [15,16], provide high sensitivity for the detection of specific exosomal miRNAs. However, these methods are incapable of heterogeneity analysis. To address these limitations, several methods have been developed for the in situ detection of exosomal miRNAs using molecular beacons [17], nano/framework beacons [18] or membrane fusion principles [19]. These strategies aim to enhance signal amplification, reduce background interference, and improve detection accuracy. However, in situ amplification of multiple exosomal miRNAs remains a significant challenge, and single-particle heterogeneity analysis of single particles is even more difficult to achieve.

To address the aforementioned limitations, we have developed a detection system based on targeted membrane fusion, enabling multiplexed, amplified visualization of tumor-derived exosomes from bladder cancer (BCa) urine samples. Compared to existing exosomal miRNA biosensing methods, our approach offers two key advantages: 1) the construction of a unique flat framework nucleic acid (ffNA) structure allows for the preparation of stable, engineered artificial vesicles (EAV), and 2) the modified EAV facilitates targeted membrane fusion and multiplexed in situ imaging of exosomal miRNAs. Leveraging this strategy, we achieved single-particle heterogeneity analysis of exosomal miRNAs and enabled accurate bladder cancer diagnosis through the combined analysis of multiple miRNA targets. This work establishes an optical imaging-based paradigm for urinary disease diagnosis based on exosomal contents.

## 2. Materials and methods

### 2.1. Cell culture

Normal urothelial cells (SV-HUC-1) and bladder cancer cell lines (5637, T24) were obtained from the Cell Bank of the Chinese Academy of Sciences (Shanghai, China). SV-HUC-1 cells were cultured in F12K medium (BasalMedia) supplemented with 10 % exosome-free fetal bovine serum (FBS, YOBIBIO) and 1 % antibiotics. 5637 and T24 cells were cultured in RPMI 1640 medium (BasalMedia) containing the same concentration of FBS and antibiotics. All cells were maintained in a humidified incubator at 37 °C with 5 % CO<sub>2</sub>.

### 2.2. Exosome isolation

Clinical samples from BCa patients and healthy donors (HD) were collected from the Shanghai Tenth People's Hospital, in strict accordance with ethical guidelines. Cell culture supernatants and morning urine samples were collected. The samples were centrifuged at 4000 rpm for 15 min at 4 °C to remove cellular debris. The supernatant was then filtered through a 0.45 µm filter, and the filtered urine was transferred to a 30 kDa ultrafiltration centrifugal tube (BIOFIL, FTT530500) for further centrifugation at 4000 rpm for 15 min at 4 °C. The concentrated urine was subsequently transferred to Eppendorf Tubes and resuspended in 100 µL phosphate buffered saline (PBS). For transmission electron microscopy (TEM) imaging, exosomes were added onto a 150-mesh formvar copper grid or indium tin oxide glass and incubated for 10 min. After washing with ultrapure water, the samples were treated with 2.5 % glutaraldehyde in PBS for 30 min and then rinsed for 15 min to fix the particles. Next, the samples were negatively stained with 2 % uranyl acetate for 10 min and rinsed for 10 min with water. Samples were dried and visualized using TEM (JEM-1400 Plus, Japan) imaging. On this basis, nanoparticle tracking analysis (NTA) was further performed to quantitatively assess the concentration of exosomes. Following resuspension in PBS, exosome samples were diluted to an appropriate concentration ( $\sim 1 \times 10^8$  particles/mL) to ensure accurate particle tracking. NTA measurements were conducted using a NanoSight NS300 instrument (Malvern Panalytical, UK) equipped with a 488 nm laser. Exosomal marker proteins, including CD9, CD81, CD63, and TSG101, as well as

the Epithelial Cell Adhesion Molecule (EpCAM), were further identified by Western blot (WB) analysis. The concentration of isolated exosomes was quantified using the bicinchoninic acid (BCA) assay, and proteins were loaded onto the gel at a concentration of 20 µg per lane for WB analysis.

### 2.3. Quantitative analysis of urinary exosomal miRNA

For exosome isolation, polyethylene glycol 6000 (PEG 6000) (40 %) was added to the sample at a 3:1 volume ratio, thoroughly mixed, and incubated at 4 °C overnight to facilitate precipitation. The mixture was then centrifuged at 15,000 ×g for 30 min at 4 °C to precipitate the exosomes. MicroRNA was subsequently isolated from the exosomes using the MiPure Cell/Tissue miRNA Kit (Vazyme). RT-qPCR was performed using the TB Green Premix Ex Taq kit (Takara) for miRNA quantification. Primer sequences used for RT-qPCR are provided in Table S1.

### 2.4. Preparation and characterization of flat framework nucleic acid (ffNA)

All DNA strands were purchased from Sangon Biotech (Shanghai, China), and the sequences are provided in Table S2. S1, S2, S3, and S4 were mixed in equal concentrations in TM buffer (10 mM Tris-HCl, 50 mM MgCl<sub>2</sub>·6H<sub>2</sub>O, pH 8.0). The mixture was rapidly heated to 95 °C and held for 10 min, followed by cooling to 4 °C for 20 min. Epithelial Cell Adhesion Molecule (EpCAM)/FAM-labeled ffNA (ffNA-3-*chol*-EpCAM/ffNA-3-*chol*-FAM), including S1-EpCAM/S1-FAM, S2-*chol*, S3-*chol*, and S4-*chol*, was prepared under the same conditions. The synthesis of ffNA, ffNA-3-*chol*, and ffNA-3-*chol*-EpCAM was confirmed by 2 % agarose gel electrophoresis. The morphology of ffNA was characterized using atomic force microscopy (AFM; SPM-9700, Shimadzu, Kyoto, Japan). 10 µL of ffNA solution was placed on freshly cleaved mica for 15 min and air-dried before imaging. Zeta potential measurements were performed using a Malvern 3000 HS laser diffraction particle size analyzer (Nano ZS, Malvern, UK).

### 2.5. Synthesis and characterization of EAV

L- $\alpha$ -Dipalmitoyl phosphatidylcholine (DPPC, MCE) was dissolved in methanol, and 1 mL of the DPPC solution (1 mg/mL) was evaporated using a rotary evaporator to remove the methanol. The residue was then hydrated with 1 mL PBS for 30 min, followed by sonication at 20 W for 1 min (6 s of sonication followed by 3 s of rest). The artificial vesicle (AV) size was measured by dynamic light scattering (DLS, Zetasizer Lab). DSN-contained EAV (EAV@DSN) was hydrated with a PBS solution containing 1 U of duplex-specific nuclease (DSN, Evrogen, Russia), 1 × DSN buffer (50 mM Tris-HCl, pH 8.0; 5 mM MgCl<sub>2</sub>; 1 mM DTT), 100 nM various molecular beacons (MBs), and 20 U of RNase inhibitors. After sonication, ffNA-3-*chol* (1 µM) was added and incubated at 37 °C for 30 min. The resulting EAV containing ffNA was subjected to ultrafiltration to remove unincorporated products. The ffNA functionalized EAV (EAV@DSN/ffNA) was further purified by ultrafiltration and dissolved in 10 mM Tris-HCl buffer (pH 7.4) containing 10 mM MgCl<sub>2</sub> for subsequent use. S1 modified with FAM and other strands modified with cholesterol were synthesized to produce ffNA with 1, 2, or 3 cholesterol modifications (ffNA-1-*chol*-FAM, ffNA-2-*chol*-FAM, ffNA-3-*chol*-FAM). The samples were then incubated with EAV, and labeling stability was assessed at different time points by flow cytometry. Single-stranded DNA modified with FAM and cholesterol (ssDNA-*chol*-FAM) served as a control group. The labeling efficiency was verified by confocal laser scanning fluorescence imaging. The encapsulation efficiency of EAV for MBs was evaluated using fluorescently labeled single-stranded oligonucleotides as a model. The fluorescence intensity was measured before ultrafiltration of the EAV solution, and subsequently measured again after complete lysis of EAV

using an equal volume of ethanol following ultrafiltration.

## 2.6. Targeted exosome fusion

The dynamic process of targeted membrane fusion was investigated using a fluorescence resonance energy transfer (FRET) decrease assay. First,  $1 \times 10^8$  exosomes were purified from urine samples and resuspended in 1 mL PBS containing 20  $\mu\text{M}$  1,1'-diiododecyl-3,3,3',3'-tetramethylindocarbocyanine perchlorate (DiI, MCE HY-D0083) and 20  $\mu\text{M}$  1,1'-diiododecyl-3,3,3',3'-tetramethylindocarbocyanine, 4-chlorobenzenesulfonate salt (DiIC<sub>18</sub>(5); DiD, MCE HY-D1028). The mixture was incubated at 37 °C for 30 min. Next, the exosomes were filtered three times at room temperature using a 100 kDa centrifugal filter (3000  $\times$ g, 10 min) to remove free dye, and the exosomes were concentrated to approximately 20  $\mu\text{L}$ . The EAV, containing  $3 \times 10^8$  particles, was mixed with DiI- and DiD-labeled exosomes. The mixture was incubated at 37 °C for 2 h to facilitate membrane fusion. Fluorescence changes during the reaction were recorded using an Infinite 200Pro microplate reader, with excitation at 480 nm. Fluorescence intensity at 580 nm and 680 nm was measured every 2 min for a total duration of 2 h. The final fluorescence spectra were obtained by exciting the samples at 480 nm, with emission spectra recorded from 514 to 850 nm using the microplate reader. The resulting mixture was dropped onto a glass slide for confocal laser scanning fluorescence imaging of membrane fusion.

## 2.7. DSN-based fluorescence amplification assay

The sequences of all miRNA targets and their corresponding MBs are provided in Table S3. The standard DSN amplification system uses a 10  $\mu\text{L}$  reaction mixture, which contains 1 $\times$  DSN buffer, 0.033 U DSN (dissolved in 25 mM Tris-HCl, pH 8.0; 50 % glycerol), 20 U RNase inhibitor, 100 nM MBs, and the miRNA target. The mixture is incubated in a thermal cycler at 37 °C for 1 h. Afterward, 10  $\mu\text{L}$  of 10 mM Ethylenediaminetetraacetic acid (EDTA) is added to inactivate the DSN enzyme, and the reaction mixture is incubated at 60 °C for an additional 5 min. The mixture is then transferred to a black 384-well microtiter plate for fluorescence signal measurement. Fluorescence emission spectra are recorded using a fluorescence microplate reader.

For the three-dimensional spectrometric method, a 60  $\mu\text{L}$  reaction mixture is prepared, containing 1 $\times$  DSN buffer, 0.2 U DSN, 120 U RNase inhibitor, 100 nM MBs, and the miRNA target. The mixture is incubated at 37 °C for 1 h. After the addition of 60  $\mu\text{L}$  of ddH<sub>2</sub>O and a 5 min incubation at 37 °C, the DSN enzyme is inactivated. The reaction mixture is transferred to a microcuvette, and fluorescence spectra are recorded using a Shimadzu RF-6000 spectrophotometer with excitation wavelengths from 300 nm to 700 nm and emission wavelengths from 400 nm to 900 nm.

## 2.8. Profiling of exosomal miRNA

To validate the application of this method for analyzing tumor-derived urinary miRNAs, EAV@DSN/fRNA-3-cholesterol-EpCAM was incubated with exosomes derived from urine at 37 °C for 2 h. The reaction mixture was then transferred to a glass slide for imaging using a confocal laser scanning fluorescence imaging microscope. Fluorescence intensity was quantified using ImageJ software.

## 2.9. Statistical analysis

Data analysis was conducted utilizing GraphPad Prism software, version 9.0. Results are expressed as the mean  $\pm$  standard deviation (SD). Statistical differences between groups were evaluated using Student's *t*-test, with a *p*-value of less than 0.05 indicating a statistically significant result. *p* > 0.05 was considered statistically not significant (n.s.), and the following denotations were used: \**p* < 0.05; \*\**p* < 0.01, \*\*\**p* < 0.001, and \*\*\*\**p* < 0.0001.

## 3. Results

### 3.1. Principle of concept

This method involves three main steps: preparation of EAV, fluorescence imaging, and statistical analysis (Fig. 1). The primary objective is to achieve the specific recognition of tumor-derived exosome subtypes and conduct multiplex in situ analysis of miRNAs within a single exosome.

A specially designed fRNA was developed to achieve more stable engineering of EAV. When the fRNA is modified with the corresponding aptamer, EAV, modified with the fRNA, acquire the ability to facilitate fusion with exosomes. The DSN enzyme exhibits unique substrate specificity, hydrolyzing only the DNA strand in dsDNA or DNA/RNA hybrid strands, regardless of the nucleotide sequence, and does not cleave single-stranded DNA or RNA. Based on this specificity, five MBs labeled with different fluorescent molecules were designed. Upon target recognition and binding, these beacons form DNA/RNA hybrid strands, which serve as substrates for DSN, leading to cleavage and the release of fluorescence signals.

The fluorescence amplification system was encapsulated inside EAV. When the EAV@fRNA recognizes and fuses with target exosomes, exchange of internal contents occurs, triggering fluorescence amplification inside the vesicles. This enables fluorescence imaging of different target miRNAs within the vesicles, allowing for the analysis of vesicle heterogeneity derived from tumor cells. By integrating these multiple targets, the system can be applied for precise diagnosis of bladder cancer.

### 3.2. Extraction and characterization of urinary exosome

Exosomes were obtained using an ultrafiltration precipitation method. Compared to ultracentrifugation, the ultrafiltration method has been shown to yield exosomes at concentrations several hundred times higher, making it an effective approach for applications with low sample input. This method is also simpler, more cost-effective, and more likely to be applicable in clinical settings. First, exosomes obtained through ultrafiltration were extensively characterized. DLS measurements showed that the particle size of exosomes extracted from the urine of BCa patients and healthy donors was  $192.22 \pm 73.87$  nm (Fig. 2a). TEM images clearly displayed a population of round and partially collapsed structures (diameter  $\approx$  110 nm), consistent with the exosome structure reported in the literature (Fig. 2b). Immunoblotting confirmed the presence of exosome-specific markers CD9, CD63, CD81, and TSG101 (Fig. 2c).

The stability of urine-derived exosomes obtained via ultrafiltration was then analyzed. DLS results over a 15-day period demonstrated that the exosomes maintained good stability during this two-week period (Fig. 2d). Additionally, the stability of miRNA encapsulated within exosomes was compared to that of free miRNA in solution. RT-qPCR results showed that miRNA inside exosomes exhibited superior stability, with nearly no degradation over two weeks, whereas free miRNA in solution degraded by approximately 70 % (Fig. 2e). In summary, all these characteristics, including size, shape, and surface protein markers, confirmed that the exosomes obtained via ultrafiltration are structurally and functionally intact. Based on previous literature and screening from databases such as TCGA, five miRNAs closely associated with BCa were selected as targets for detection, including miR-21, miR-96, miR-183, miR-205, and miR-210. The relevant miRNAs and their functions are provided in Table S4. The analysis of the expression levels of these five targets in cancerous and adjacent normal tissues in the TCGA database further supports this observation (Fig. 2f).

### 3.3. Design and functional characterization of fRNA

Engineering vesicles with cholesterol-modified single-stranded DNA (ssDNA-cholesterol) is a widely used technique; however, it presents several

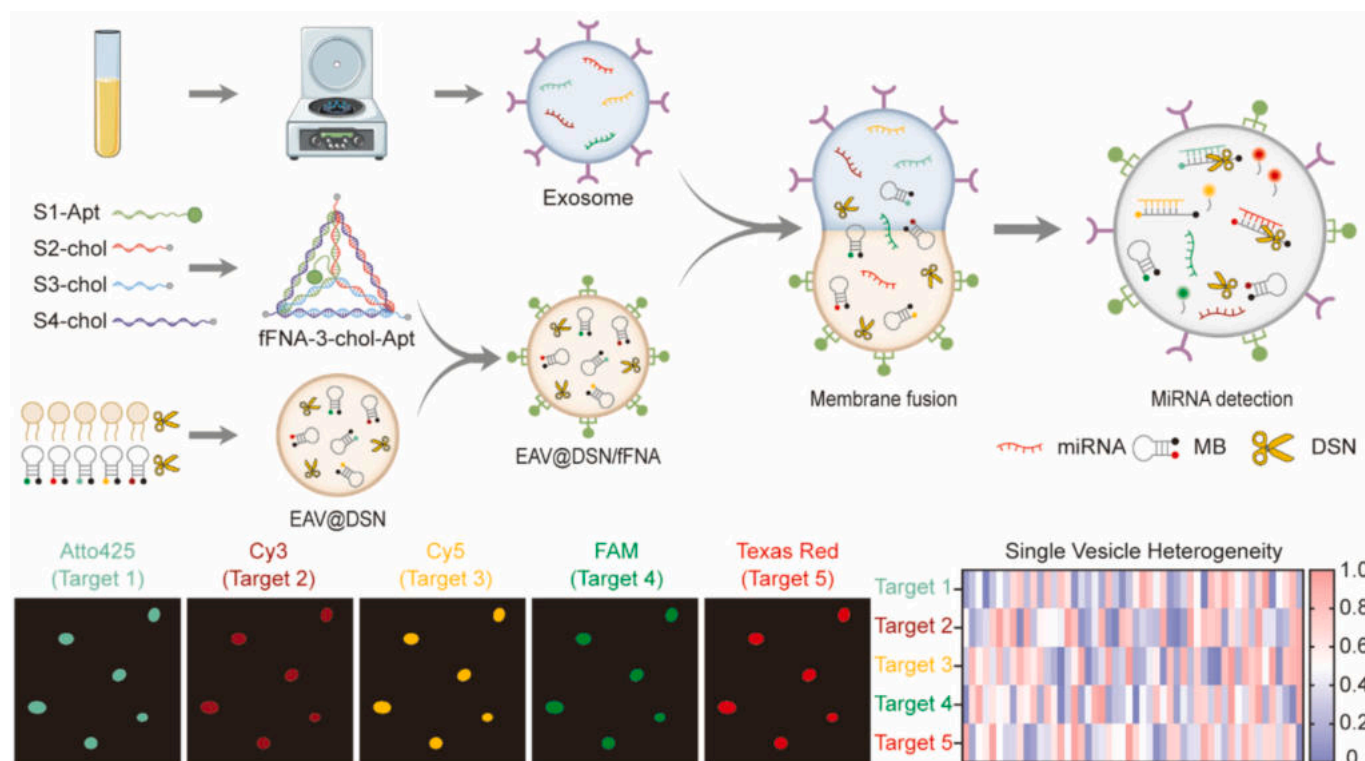


**Fig. 1.** Schematic of in situ multiplex miRNA analysis and single vesicle heterogeneity analysis. The analytical workflow consists of three steps: (1) Collection of exosomes from clinical urine samples. (2) Preparation of engineered artificial vesicles (EAV). (3) In situ multiplex imaging of target urinary exosomal miRNAs and data analysis.

significant challenges, such as easy detachment and unpredictable endocytosis. Recent efforts have explored the use of fFNA, such as DNA tetrahedra, for vesicle engineering. While DNA tetrahedra, as a 3D structural material, offer the advantage of cell and exosome entry, concerns remain about their direct internalization into exosomes [20]. In contrast to DNA tetrahedra, fFNA is more likely to adhere to the membrane, offering a potential solution to these challenges [21]. Therefore, to enhance the stability of artificial vesicle engineering and minimize the risk of unpredictable endocytosis, we designed fFNA (Fig. 3a).

Using a one-pot annealing method, fFNA, fFNA-3-chole, and fFNA-3-chole-EpCAM (the latter modified with three cholesterol modifications and the EpCAM aptamer) were directly synthesized with or without cholesterol modification on S1/S2/S3/S4. The 2 % agarose gel electrophoresis image clearly shows distinct bands for different single-stranded and fFNA constructs, confirming the successful synthesis of fFNA, fFNA-3-chole, and fFNA-3-chole-EpCAM (Fig. 3b). In Fig. 3b, the appearance of two bands in the S2-only lane is likely attributable to conformational heterogeneity or self-complementarity of ssDNA under non-denaturing electrophoretic conditions. Similar phenomena have been reported in the literature when studying structured or self-complementary ssDNA sequences [22,23]. The Zeta potential of fFNA was  $-11.9 \pm 1.54$  mV (Fig. S1). Morphologically, AFM images showed that fFNA at pH 8 presented uniform nanoparticles with a diameter ranging from 10 to 20 nm, and a peak height of 2 nm (Fig. S2). This is consistent with the theoretical width of the DNA double helix structure, confirming that fFNA adopts a flat conformation. To prepare EAV, DPPC liposome solution was subjected to sonication, and their morphology was observed using TEM (Fig. S3a). DLS measurements were conducted over 8 days to assess the particle size stability of the EAV, showing that the particle size remained stable over one week (Fig. 3c), making them suitable as reliable vesicle delivery carriers.

During the one-pot synthesis of fFNA-3-chole, the DNA strand S1 was

modified with a FAM fluorescent label to produce fFNA-3-chole-FAM, allowing its fluorescence signal to evaluate the labeling efficiency and stability of the fFNA. Various fFNA constructs with different numbers of cholesterol modifications were synthesized and named accordingly as fFNA-0-chole, fFNA-1-chole, fFNA-2-chole, and fFNA-3-chole. First, flow cytometry was used to evaluate the stability of EAV labeled with fFNA constructs modified with different numbers of cholesterol moieties. The experimental results showed that only fFNA-3-chole maintained stable labeling efficiency over 4 days, with an efficiency of 98.6 % (Fig. 3d,e), highlighting the exceptional performance of fFNA-3-chole in the stable functionalization of vesicles. To further evaluate the modification stability of EAV, we extended the observation period and compared the stability of ssDNA and fFNA-3-chole over a 7-day period (Fig. S4). The results demonstrated that fFNA-3-chole exhibited significantly enhanced stability compared to the commonly used EAV anchoring molecule ssDNA. Next, DiI staining was performed on EAV, and the products were subjected to ultrafiltration to remove unbound substances. fFNA constructs with 0, 1, and 2 cholesterol modifications, as well as ssDNA-chole-FAM, were co-incubated with DiI-labeled EAV. Confocal imaging was used to assess the labeling efficiency of these constructs on EAV (Fig. 3f), revealing that fFNA-3-chole-FAM and ssDNA-chole-FAM exhibited the highest labeling efficiencies of 93.59 % and 93.74 %, respectively (Fig. 3g). In summary, a flat framework nucleic acid was synthesized, which not only demonstrated a labeling efficiency of up to 93 %, comparable to that of ssDNA-chole in EAV labeling, but also maintained an exceptionally high labeling stability.

### 3.4. Targeted membrane fusion

EpCAM, a homophilic cell-cell adhesion glycoprotein, is a well-known tumor antigen that is overexpressed in BCa [24,25] and was selected as a specific target for exosome fusion. First, the differential expression of EpCAM in exosomes derived from BCa and HD was



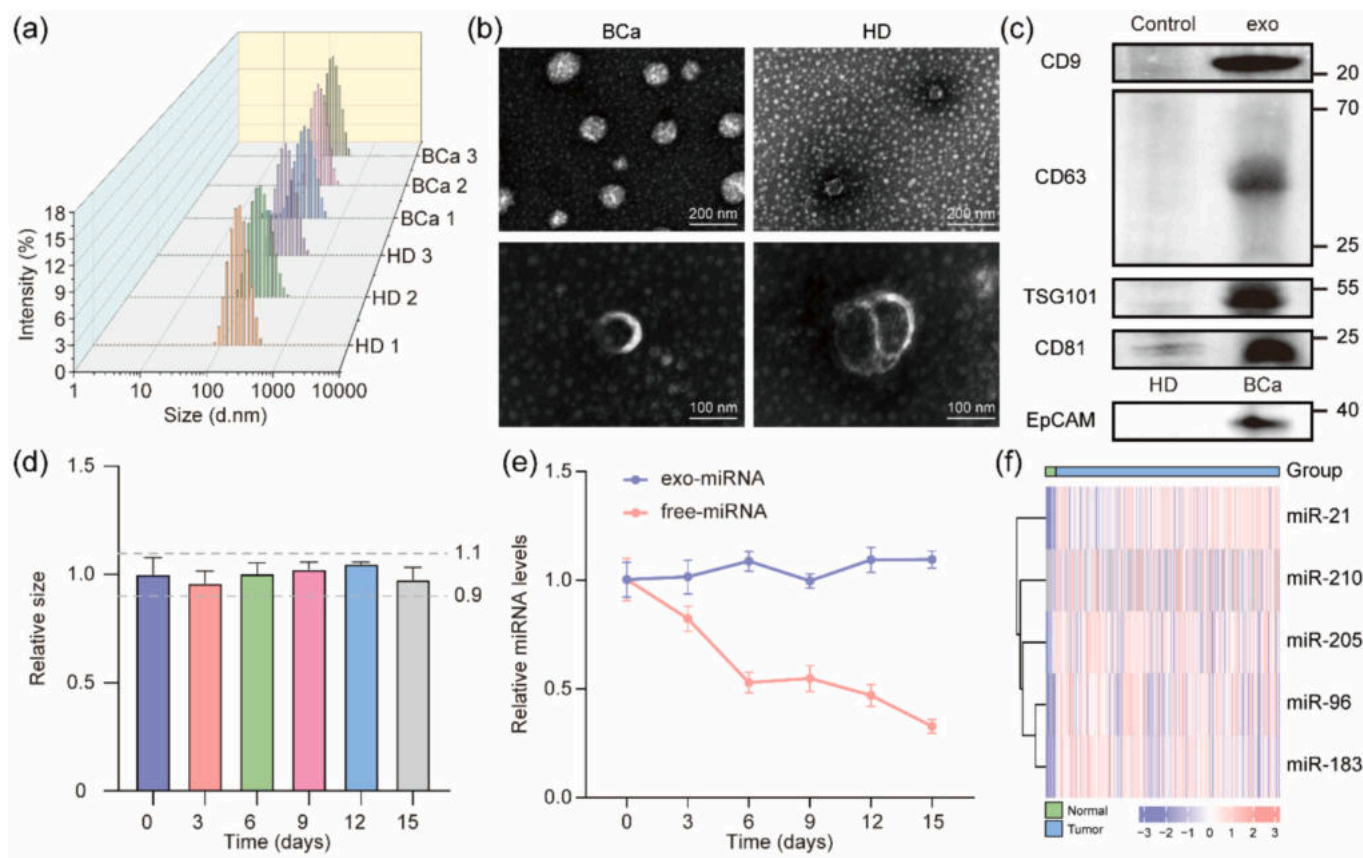


**Fig. 2.** Preparation and characterization of urinary exosomes. (a and b) Characterization of exosomes derived from BCa and HD by DLS (a), and TEM imaging (b). (c) Characterization of exosomes by Western blotting. (d) Evaluation of the particle size stability of exosomes at different time points ( $n = 3$ ). (e) Comparison of the stability of free miR-21 in solution and exosomal miR-21 in exosomes using RT-qPCR ( $n = 4$ ). (f) Relative expression level analysis of five miRNAs in BCa tissues and their adjacent normal tissues based on TCGA database.

validated by WB analysis (Fig. 2c). To investigate whether fFNA can guide the fusion of EAV and exosomes after functionalization, we first conjugated an EpCAM aptamer (fFNA-3-*chol*-EpCAM) to the S1 to target tumor-derived exosomes. Membrane fusion was monitored using FRET techniques. As shown in the schematic diagram (Fig. 4a), exosomes were dual-labeled with DiI and DiD in a FRET dequenching assay. Following membrane fusion, the membrane area expanded, leading to a decrease in the FRET efficiency between DiD and DiI on the membrane surface. Using EAV functionalized or not with fFNA for comparison, exosome+DiD/DiI incubated with EAV lacking fFNA-3-*chol*-EpCAM exhibited minimal fusion (Fig. 4b). A dynamic membrane diffusion monitoring experiment was also performed in the FRET assay. When non-fluorescent EAV was incubated with dual-labeled exosomes-DiD/DiI, the DiI signal increased rapidly while the DiD signal simultaneously decreased, reaching a plateau after approximately 2 h (Fig. 4c). TEM images also identified vesicles in the intermediate state of fusion (Fig. S3b). These results confirmed that fFNA-3-*chol*-EpCAM successfully mediated fusion between EAV and exosomes, reaching a plateau within 2 h.

To further validate the effectiveness of membrane fusion, EAV@fFNA-3-*chol*-EpCAM and exosomes from urine of bladder cancer patients were labeled with DiI and DiO, respectively. The DiI and DiO fluorescence markers co-localized well. In contrast, no detectable co-localized fluorescence signals were observed in the group of EAV without fFNA-3-*chol*-EpCAM modification and exosomes derived from BCa, as well as in the group of EAV modified with fFNA-3-*chol*-EpCAM and exosomes derived from normal healthy human urine (Fig. 4d). These results demonstrated that fFNA not only stably functionalized EAV but also successfully mediated targeted membrane fusion between

EAV and exosomes, enabling the use of encapsulated miRNA detection probes for downstream analysis.

### 3.5. DSN-based orthogonal miRNA detection

In the fluorescence amplification system, the enzymatic activity of DSN was utilized, which specifically cleaves DNA sequences in DNA-RNA heteroduplexes without affecting RNA sequences. These unique enzymatic cleavage properties make DSN an excellent choice for detecting miRNA and constructing cDNA (24). MBs labeled with different fluorescent molecules were designed for various miRNA targets. When the MBs bind to the target miRNA, they are recognized by DSN as part of a DNA-RNA heteroduplex, leading to cleavage of the MB molecules, releasing the fluorescent molecules and the uncleaved target miRNA. The target miRNA then binds to the next MB molecule, generating a cyclic process that continuously amplifies the fluorescence signal (Fig. 5a). miRNA-21, a widely elevated biomarker in various types of cancer, was selected as the target model to validate the fluorescence amplification strategy. To evaluate the performance of the fluorescence amplification system, the feasibility of the method was first assessed (Fig. 5b). The results indicate that amplification of the fluorescence signal highly depends on the combined action of miRNA, DSN, and MB. Stronger fluorescence was observed under 5 mM  $Mg^{2+}$  conditions, revealing the optimal reaction conditions for the detection system. Subsequently, different MBs were designed for various target miRNAs, and the results showed that fluorescence amplification was successfully achieved for all five target miRNAs (Fig. 5c), confirming the versatility of the DSN amplification strategy. Taking miRNA-21 as an example, the calculated detection limit was 0.6 nM (Fig. 5d). Moreover, the anti-

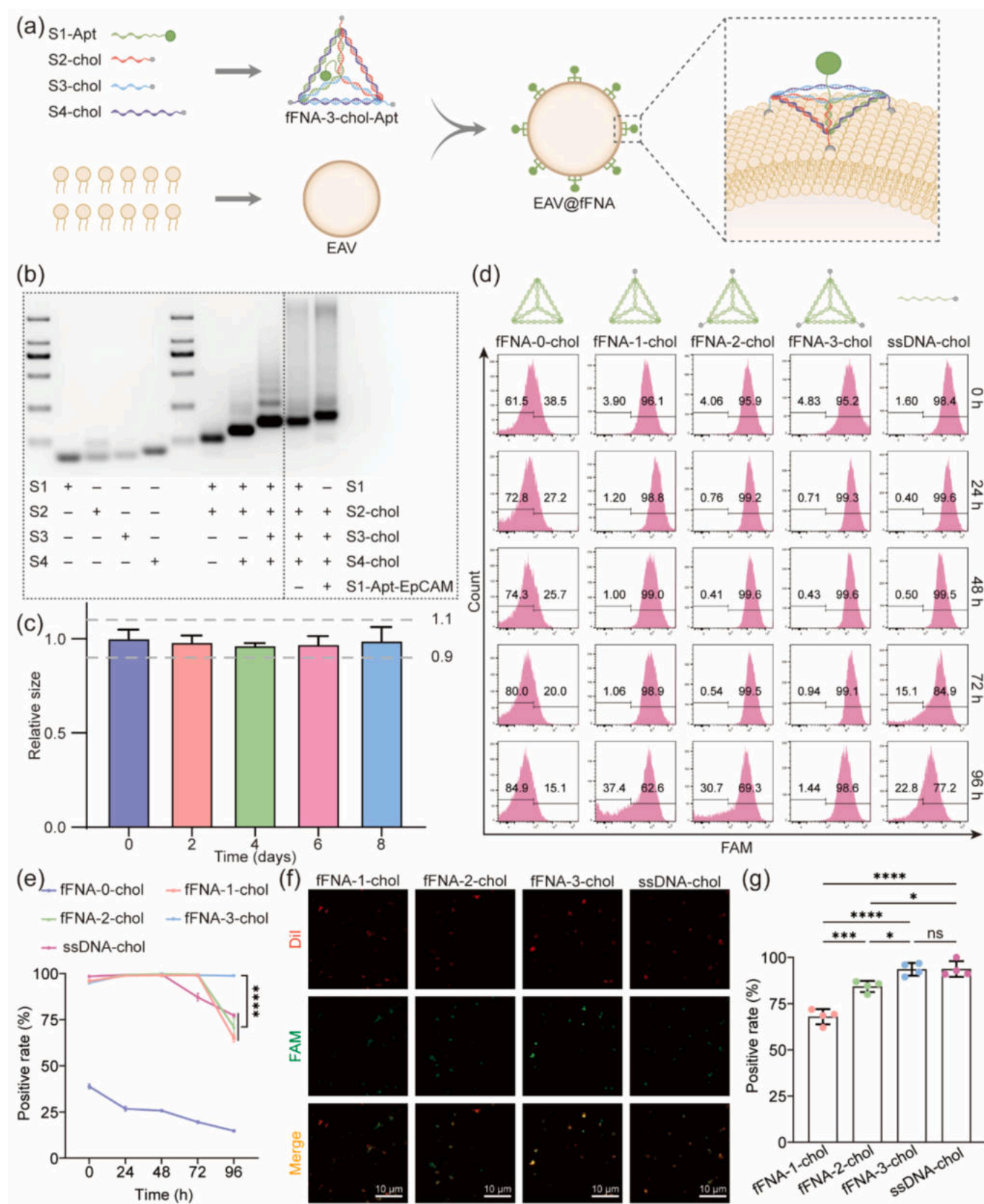


**Fig. 3.** Preparation and functional evaluation of fFNA. (a) Schematic illustration of the construction of fFNA and engineered EAV. (b) Validation of the assembly of fFNA, fFNA-3-choI, fFNA-3-choI-EpCAM, and single-stranded S1 - S4 based on 2 % agarose gel electrophoresis. (c) Particle size stability of EAV at different time points (n = 3). (d and e) Stability of EAV constructed using different components. Data were collected using flow cytometry (n = 3). (f and g) Evaluation of the engineering efficiency of EAV constructed using different components. EAV was stained with DiI (n = 4). \* $p < 0.05$ ; \*\* $p < 0.01$ ; \*\*\* $p < 0.001$ , and \*\*\*\* $p < 0.0001$ .

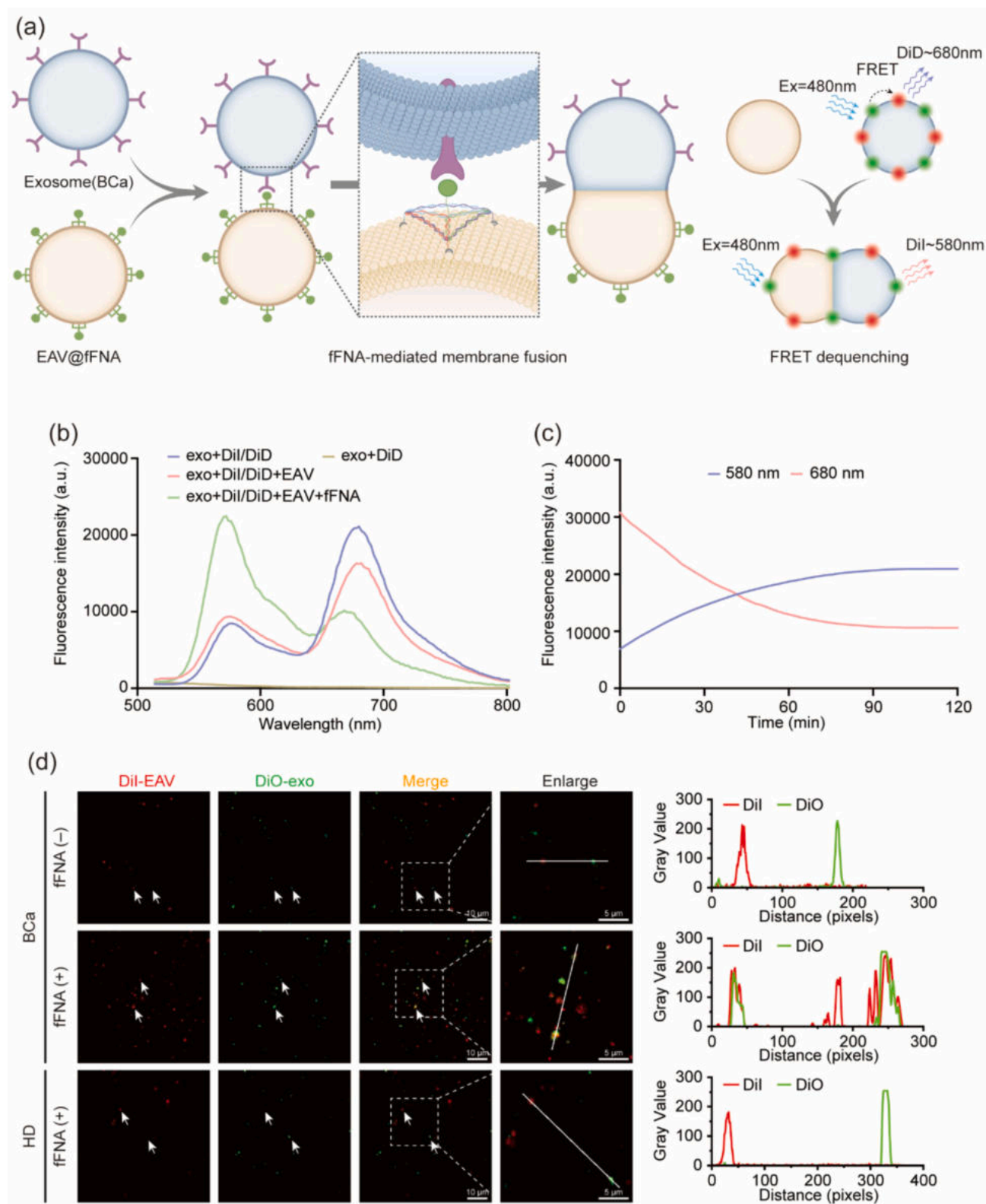


**Fig. 4.** fFNA-mediated membrane fusion. (a) Schematic illustration of fFNA-mediated membrane fusion and membrane fusion-based fluorescence resonance energy transfer (FRET). The fusion event was measured by the decreased FRET efficiency between the donor (DiI, 580 nm) and acceptor (DiD, 680 nm). (b) Fluorescence spectroscopic analysis of the fusion between EAV@fFNA, EAV, and the dual-labeled exosomes. Exo + DiI/DiD and Exo + DiD were used as controls. (c) Fluorescence kinetic analysis of the fusion between EAV@fFNA and DiD/DiI dual-labeled exosomes, measuring the changes in fluorescence intensity at 580 nm and 680 nm over a 2-h period. (d) Confocal imaging and fluorescence intensity analysis were performed to assess the fusion of exosomes derived from BCa patients with EAV, which was modified with or without fFNA. The fusion reactions between EAV and exosomes from healthy donors (HD) were used as controls. EAV was labeled with DiI, and urine-derived exosomes were labeled with DiO. Fluorescence intensity was quantified as gray scale values using ImageJ software.



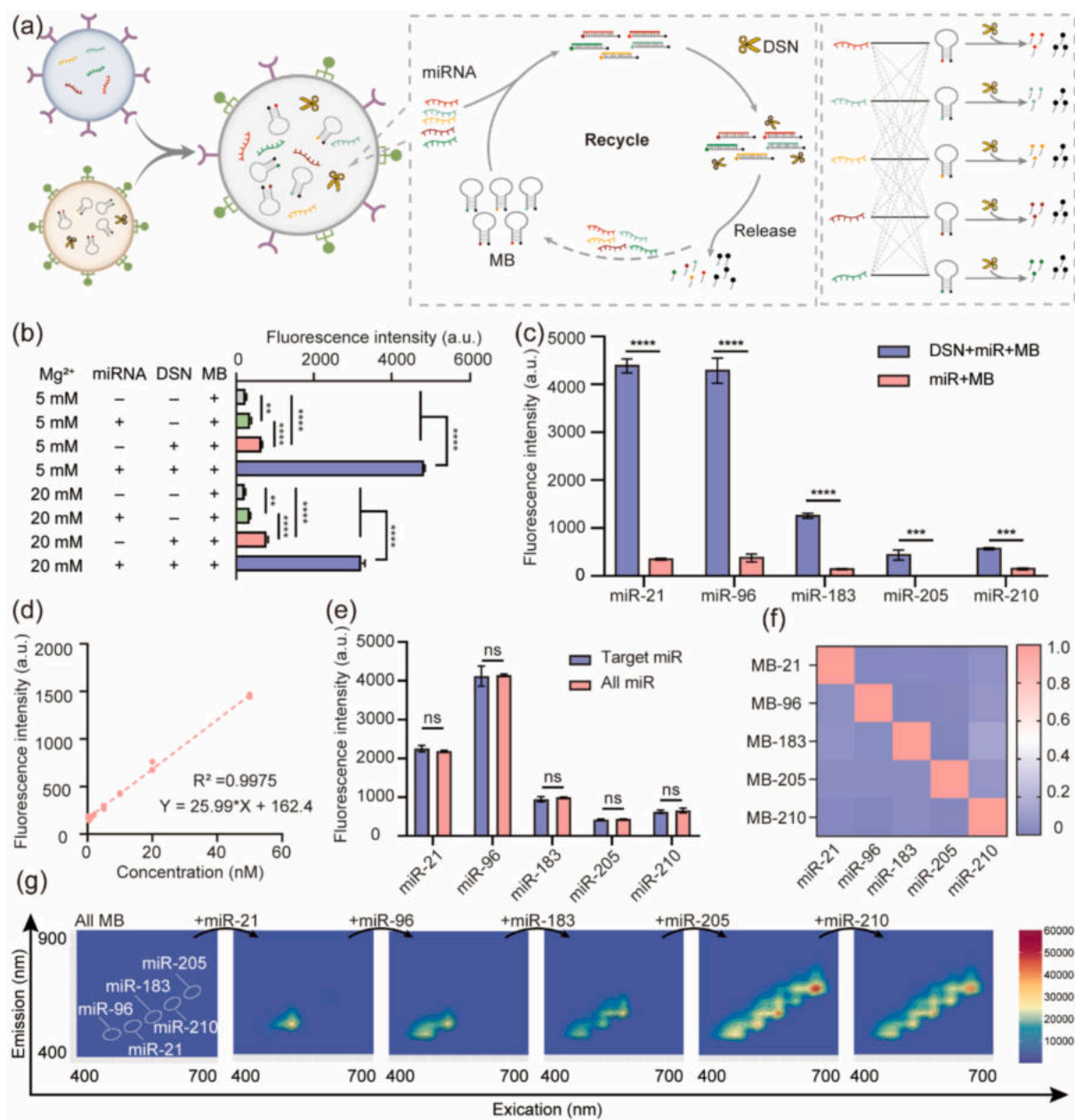


**Fig. 5.** Construction of orthogonal detection system. (a) Schematic illustration of the DSN-based orthogonal miRNA detection system after membrane fusion. (b) Feasibility assessment of the reaction system. (c) Validation of the universality of the miRNA detection system. (d) Validation of the sensitivity of the miRNA detection system. (e) Evaluation of the anti-interference capability of the detection system. Fluorescence intensity in the presence or absence of interfering miRNAs was measured. (f) Assessment of the specificity and cross-reactivity of the detection system. (g) Responsiveness of the detection system to the miRNA targets. Three-dimensional spectral results were collected in the presence of different miRNA target combinations. \* $p < 0.05$ ; \*\* $p < 0.01$ , \*\*\* $p < 0.001$ , and \*\*\*\* $p < 0.0001$ .

interference capability of the DSN system was validated. As shown in Fig. 5e, the inclusion of interfering miRNA in the target mixture did not affect the detection signal, demonstrating the system's resistance to interference. Further three-dimensional fluorescence spectroscopy was employed to evaluate the effect of introducing multiple potentially interfering MBs in the presence of a single target. The aim was to investigate whether the selected fluorescent probes would affect the detection of the single target. After normalization, the results showed no significant decrease or aberration in fluorescence intensity or signal characteristics when multiple MBs coexisted, indicating minimal or negligible quenching effects (Fig. S5a). The orthogonality of the detection system was assessed by measuring the fluorescence signals of five target miRNAs (Fig. 5f). Each miRNA was tested with its corresponding probe, and minimal cross-reactivity was observed, confirming the

system's high specificity and reliability for simultaneous miRNA detection. In addition, three-dimensional spectroscopy was used to characterize the fluorescence amplification results in the presence of different target combinations, further demonstrating the superior performance of the DSN-based amplification system (Fig. 5g). The encapsulation efficiency of MBs by EAV was further investigated, and the results demonstrated that EAV achieved an encapsulation efficiency of approximately 20 % (Fig. S5b). Therefore, a DSN-based amplification system with excellent orthogonality and strong anti-interference capability has been developed.

### 3.6. Urinary exosomal miRNA heterogeneity analysis and BCa diagnosis

Then, the feasibility of the overall approach was validated on



exosomes derived from cells. Two bladder cancer cell lines, 5637 and T24, as well as a normal urinary epithelial cell line, SV-HUC-1, were selected. RT-qPCR was used to compare the overall expression of five target miRNAs in exosomes (Fig. 6a). The results showed that miRNA expression in exosomes from BCa cell lines was generally higher than that in exosomes from normal urinary epithelial cells. However, statistical analysis of miRNA-21 and miRNA-96 in exosomes from the 5637 cell line showed no significant difference compared to the SV-HUC-1 group. Next, fluorescence imaging was performed on the fused exosomes (Fig. 6b), revealing distinct fluorescence differences both between different cell lines and within the same cell line. Statistical analysis of the overall fluorescence intensity (Fig. 6c) showed that, in contrast to the RT-qPCR results, exosomes from the 5637 cell line exhibited

significantly higher levels of miRNA-21 and miRNA-96 compared to the SV-HUC-1 cell line. This can be attributed to the targeted membrane fusion, which reduced the background fluorescence in the SV-HUC-1 group, while exosomes from the 5637 cell line, which express EpCAM, could be effectively detected. Additionally, the fluorescence differences within individual vesicles were used to analyze the heterogeneity among exosomes. Thirty fused vesicles were selected from imaging results of different cell lines for heterogeneity analysis, as shown in Fig. 6d. The results revealed that exosomes from the same cell source exhibit different miRNA expression profiles within individual vesicles, highlighting the heterogeneity of exosomes from a single cellular origin. In summary, the feasibility of applying this approach for in situ exosome imaging detection was confirmed, and it also revealed the heterogeneity

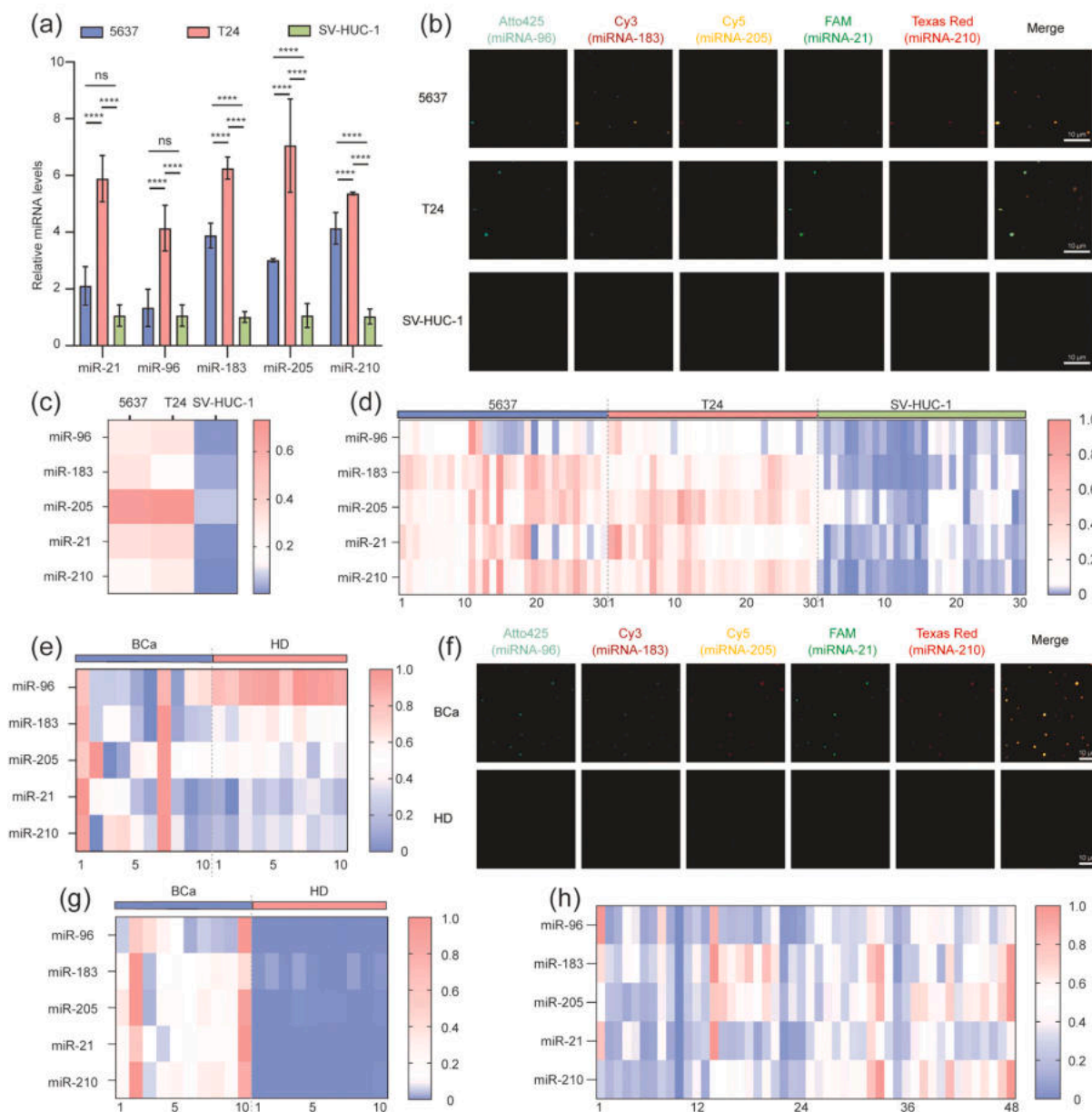


**Fig. 6.** Analysis of urinary exosomal miRNA heterogeneity and its application in BCa diagnosis. (a) Expression levels of five target miRNAs in three cell lines ( $n = 3$ ). (b) Confocal imaging images of the in situ multiplex detection results of miRNAs in exosomes derived from three cell sources. Analysis of miRNA expression heterogeneity (c) and single-vesicle heterogeneity (d) in 3 cell lines. For each cell line, 30 vesicles were randomly selected for analysis. (e) Expression levels of five target miRNAs in exosomes derived from 20 clinical urine samples ( $n = 4$ ). (f) Confocal imaging images of the in situ multiplex detection results of miRNAs in exosomes derived from BCa and HD samples. Analysis of miRNA expression heterogeneity (g) and single-vesicle heterogeneity (h) in clinical samples. Single-vesicle heterogeneity analysis was conducted on the imaging results of one BCa patient, with a total of 48 vesicles selected. \* $p < 0.05$ ; \*\* $p < 0.01$ , \*\*\* $p < 0.001$ , and \*\*\*\* $p < 0.0001$ .

of individual exosomes from the same cell source.

Next, the system was applied to the detection of actual urine samples. A total of 20 urine samples were collected (10 from BCa patients and 10 from healthy donors, HD). After isolating exosomes via ultrafiltration, RT-qPCR was first performed to measure the levels of five miRNAs (Fig. 6e). The results showed that the overall level of miR-96 in the HD group was higher than that in the BCa group. Subsequently, fluorescence imaging was conducted using functionalized EAV (Fig. 6f). Overall fluorescence intensity analysis of the different samples (Fig. 6g) revealed that the fluorescence intensity of all five targets in the BCa group was significantly higher than that in the HD group. This can be attributed to the targeted fusion effect of the fFNA-modified engineered artificial vesicles, which eliminated interference from exosomes not expressing EpCAM and their internal targets. Next, the heterogeneity of exosomes derived from bladder cancer patients was investigated (Fig. 6h). Similar to the cellular level, exosomes derived from tumor cells expressing EpCAM exhibited different miRNA expression profiles. To further validate the feasibility of the detection platform, an additional set of 20 clinical samples was collected and tested (Fig. S6). The results were consistent with the previous findings, demonstrating the stability of the platform. Clinical information for all 40 samples is summarized in Table S5. Fluorescence imaging results were used to jointly diagnose BCa with five miRNAs, and ROC analysis demonstrated excellent diagnostic performance (Fig. S7a). The confusion matrix showed 100 % specificity and accuracy in the validation cohort for distinguishing BCa from HD (Fig. S7b). These comparative results further demonstrate that our method exhibits superior diagnostic performance for urine-derived exosomes and can reveal the heterogeneity of exosomes originating from urine.

#### 4. Discussion

The examination of urine exosomal content is a promising approach for the clinical diagnosis and recurrence monitoring of bladder cancer. Additionally, in situ analysis of exosomal contents derived from bladder cancer could help eliminate interference from other exosomes, offering unique insights into exosome heterogeneity. However, in situ multiplex exosomal content analysis has remained an extremely challenging task. In this study, we modified artificial vesicles using a two-dimensional fFNA method to construct EAV capable of targeted membrane fusion with bladder cancer-derived exosomes. By leveraging the unique catalytic properties of DSN, we achieved orthogonal and amplified detection of exosomal content. Using five bladder cancer diagnostic miRNAs as examples, we not only analyzed the heterogeneity of individual exosomes, but also achieved 100 % sensitivity and specificity in bladder cancer diagnosis. Only 5 miRNAs were chosen to be analyzed simultaneously in this work, as it is close to the upper limit of fluorescence differentiation ability of conventional imaging devices. In scenarios requiring additional target diversity, this method can be further integrated with DNA computing.

This engineering method, based on two-dimensional fFNA, demonstrates greater stability compared to ssDNA-chol and overcomes potential issues related to three-dimensional frame nucleic acid passing through membranes. It may serve as a paradigm for the engineering design of various vesicle-based detection platforms. Moreover, the DSN-based orthogonal detection system are theoretically compatible with in situ detection of a range of RNA targets, including mRNA, lncRNA, circRNA, and sncRNA. It can be speculated that this approach could enable synergistic analysis of different biomarkers. However, it is important to note that current limitations remain in the field of in situ multiplex detection of proteins and small molecules.

Overall, in membrane fusion-based in situ detection systems, each exosome can be regarded as a naturally constructed, independent microreactor. Owing to the highly enclosed membrane structure, this confined reaction environment effectively prevents contamination from external sources and eliminates signal interference between different

exosomes during the detection process. Such isolated reaction compartments provide an ideal platform for high-sensitivity and high-specificity single-vesicle analysis. Furthermore, assuming that the exosome is a perfect spherical structure containing only a single target molecule, a 100 nm-diameter exosome would enclose an internal volume of approximately 0.524 aL, corresponding to a local effective concentration of approximately 3.17  $\mu$ M. In our previous validation experiments, the DSN-based fluorescence detection system demonstrated a detection limit of 0.6 nM under solution-phase conditions, which is sufficient to detect a single target molecule. This effect of achieving “high local concentration” within an extremely small space not only significantly enhances detection sensitivity but also lays a theoretical foundation for single-molecule level analysis.

The expression level of EpCAM on exosomes, which mediates membrane fusion in this study, may potentially influence the fusion efficiency between EAV and target exosomes. However, encouraging results were obtained, as no apparent false-negative outcomes attributable to EpCAM expression levels were observed across multiple clinical samples. To overcome this potential limitation, future studies are planned to incorporate a multi-target fusion strategy, such as the combined recognition of CD9, CD63, or other tumor-specific membrane proteins, in order to enhance the applicability and robustness of the detection system in heterogeneous samples. Therefore, despite the presence of potential limitations, this study demonstrates promising prospects in targeted detection, and heterogeneity analysis, indicating substantial potential for further in-depth exploration.

#### CRediT authorship contribution statement

**Yang Wang:** Conceptualization, Writing – original draft. **Huaxing Li:** Conceptualization, Writing – original draft. **Xiangqian Cao:** Investigation. **Weiguang Zhao:** Writing – review & editing. **Hongquan Gou:** Data curation, Writing – review & editing. **Chenkai Yang:** Methodology. **Haoyuan Wang:** Data curation. **Jie Deng:** Formal analysis. **Wen Chen:** Project administration. **Haipeng Qi:** Software. **Dongsheng Mao:** Conceptualization, Supervision. **Xiaoli Zhu:** Supervision. **Bing Shen:** Supervision.

#### Declaration of competing interest

The authors declare that they have no known competing financial interests or personal relationships that could have appeared to influence the work reported in this paper.

#### Acknowledgements

This work was supported by the National Key Research and Development Program of China, Grant/Award Number: 2023YFC2606100; the National Natural Science Foundation of China, Grant/Award Number: 22074090, 32371531, 32301256, 82072821; Medical Innovation Research Special Project of the Shanghai Science and Technology Innovation Action Plan, Grant/Award Number: 23Y11907900; the Natural Science Foundation of Shanghai Municipality, Grant/Award Number: 23ZR1449100, 23ZR1446000; the Shanghai Sailing Program, Grant/Award Number: 23YF1432600; the Shanghai Municipal Health Commission, Grant/Award Number: 20244Z0020, 20234Y0005; the National Institute of Hospital Administration, Grant/Award Number: JYHRJG2024B46.

#### Appendix A. Supplementary data

Supplementary data to this article can be found online at <https://doi.org/10.1016/j.cej.2025.168311>.

## Data availability

Data will be made available on request.

## References

- [1] A. Lopez-Beltran, M.S. Cookson, B.J. Guercio, L. Cheng, Advances in diagnosis and treatment of bladder cancer, *BMJ-BRITISH MEDICAL JOURNAL* 384 (2024) e076743, <https://doi.org/10.1136/bmj-2023-076743>.
- [2] E. Compérat, M.B. Amin, R. Cathomas, A. Choudhury, M. De Santis, A. Kamat, A. Stenzl, H.C. Thoeny, J.A. Witjes, Current best practice for bladder cancer: a narrative review of diagnostics and treatments, *LANCET* 400 (10364) (2022) 1712–1721, [https://doi.org/10.1016/S0140-6736\(22\)01188-6](https://doi.org/10.1016/S0140-6736(22)01188-6).
- [3] M. Babjuk, M. Burger, O. Capoun, D. Cohen, E.M. Compérat, J.L.D. Escrig, P. Gontero, F. Liedberg, A. Masson-Lecomte, A.H. Mostafid, J. Palou, B.W.G. van Rhijn, M. Roupriat, S.F. Shariat, T. Seisen, V. Soukup, R.J. Sylvester, European Association of Urology guidelines on non-muscle-invasive bladder Cancer (ta, T1, and carcinoma in situ), *Eur. Urol.* 81 (1) (2022) 75–94, <https://doi.org/10.1016/j.eururo.2021.08.010>.
- [4] T.W. Flaig, P.E. Spiess, M. Abern, N. Agarwal, R. Bangs, S.A. Boorjian, M. K. Buyyounouski, K. Chan, S. Chang, T. Friedlander, R.E. Greenberg, K.A. Guru, H. W. Herr, J. Hoffman-Censits, A. Kishan, S. Kundu, S.M. Lele, R. Mamtani, V. Margulis, O.Y. Mian, J. Michalski, J.S. Montgomery, L. Nandagopal, L. C. Pagliaro, M. Parikh, A. Patterson, E.R. Plimack, K.S. Pohar, M.A. Preston, K. Richards, W.J. Sexton, A.O. Siefker-Radtke, M. Tollefson, J. Tward, J.L. Wright, M.A. Dwyer, C.J. Cassara, L.A. Gurski, Bladder cancer, version 2.2022 featured updates to the NCCN guidelines, *J. Natl. Compr. Cancer Netw.* 20 (8) (2022) 866–878, <https://doi.org/10.6004/jnccn.2022.0041>.
- [5] T.J. Oh, J.Y. Lee, Y. Seo, M.A. Woo, J.S. Lim, Y.G. Na, K.H. Song, B.R. Bang, J. J. Lee, J.H. Shin, S. An, Evaluation of sensitive urine DNA-based *PENK* methylation test for detecting bladder Cancer in patients with hematuria, *J. Mol. Diagn.* 25 (9) (2023) 646–654, <https://doi.org/10.1016/j.jmol.2023.05.003>.
- [6] W.M. Ruan, X. Chen, M. Huang, H. Wang, J.X. Chen, Z.X. Liang, J.T. Zhang, Y. Q. Yu, S. Chen, S.Z. Xu, T.L. Hu, X. Li, Y.J. Guo, Z.Y. Jiang, Z.W. Chen, J. Huang, T. X. Lin, J.B. Fan, A urine-based DNA methylation assay to facilitate early detection and risk stratification of bladder cancer, *Clin. Epigenetics* 13 (1) (2021) 91, <https://doi.org/10.1186/s13148-021-01073-x>.
- [7] P.G. Moon, S. You, J.E. Lee, D. Hwang, M.C. Baek, Urinary exosomes and proteomics, *Mass Spectrom. Rev.* 30 (6) (2011) 1185–1202, <https://doi.org/10.1002/mas.20319>.
- [8] M. Maas, T. Todenhöfer, P.C. Black, Urine biomarkers in bladder cancer - current status and future perspectives, *Nat. Rev. Urol.* 20 (10) (2023) 597–614, <https://doi.org/10.1038/s41585-023-00773-8>.
- [9] N. Mahtal, O. Lenoir, C. Tinel, D. Anglicheau, P.L. Tharaux, MicroRNAs in kidney injury and disease, *Nat. Rev. Nephrol.* 18 (10) (2022) 643–662, <https://doi.org/10.1038/s41581-022-00608-6>.
- [10] D. Santovito, C. Weber, Non-canonical features of microRNAs: paradigms emerging from cardiovascular disease, *Nat. Rev. Cardiol.* 19 (9) (2022) 620–638, <https://doi.org/10.1038/s41569-022-00680-2>.
- [11] Z. Andreu, R.O. Oshiro, A. Redruello, S. López-Martín, C. Gutiérrez-Vázquez, E. Morato, A.I. Marina, C.O. Gómez, M. Yáñez-Mó, Extracellular vesicles as a source for non-invasive biomarkers in bladder cancer progression, *Eur. J. Pharm. Sci.* 98 (2017) 70–79, <https://doi.org/10.1016/j.ejps.2016.10.008>.
- [12] K. Matsuzaki, K. Fujita, K. Jingushi, A. Kawashima, T. Ujike, A. Nagahara, Y. Ueda, G. Tanigawa, I. Yoshioka, K. Ueda, R. Hanayama, M. Uemura, Y. Miyagawa, K. Tsujikawa, N. Nonomura, MiR-21-5p in urinary extracellular vesicles is a novel biomarker of urothelial carcinoma, *ONCOTARGET* 8 (15) (2017) 24668–24678, <https://doi.org/10.18632/oncotarget.14969>.
- [13] B. Pardini, F. Cordero, A. Naccarati, C. Viberti, G. Birollo, M. Oderda, C. Di Gaetano, M. Arigoni, F. Martina, R.A. Calogero, C. Sacerdote, P. Gontero, P. Vineis, G. Matullo, microRNA profiles in urine by next-generation sequencing can stratify bladder cancer subtypes, *Oncotarget* 9 (29) (2018) 20658–20669, <https://doi.org/10.18632/oncotarget.25057>.
- [14] X.M. Jiang, L.T. Du, L.L. Wang, J. Li, Y.M. Liu, G.X. Zheng, A.L. Qu, X. Zhang, H. W. Pan, Y.M. Yang, C.X. Wang, Serum microRNA expression signatures identified from genome-wide microRNA profiling serve as novel noninvasive biomarkers for diagnosis and recurrence of bladder cancer, *Int. J. Cancer* 136 (4) (2015) 854–862, <https://doi.org/10.1002/ijc.29041>.
- [15] B. Ning, Z. Huang, B.M. Youngquist, J.W. Scott, A. Niu, C.M. Bojanowski, K. J. Zvezdaryk, N.S. Saba, J. Fan, X.M. Yin, J. Cao, C.J. Lyon, C.Z. Li, C.J. Roy, T. Y. Hu, Liposome-mediated detection of SARS-CoV-2 RNA-positive extracellular vesicles in plasma, *Nat. Nanotechnol.* 16 (9) (2021) 1039–1044, <https://doi.org/10.1038/s41565-021-00939-8>.
- [16] W.S. de Voogt, M.E. Tanenbaum, P. Vader, Illuminating RNA trafficking and functional delivery by extracellular vesicles, *Adv. Drug Deliv. Rev.* 174 (2021) 250–264, <https://doi.org/10.1016/j.addr.2021.04.017>.
- [17] F. Zhou, L. Pan, X.W. Ma, J. Ye, Z.H. Xu, C.Q. Yuan, C.Z. Shi, D.L. Yang, Y. Luo, M. Li, P.F. Wang, In situ, fusion-free, multiplexed detection of small extracellular vesicle miRNAs for cancer diagnostics, *Anal. Chem.* 96 (39) (2024) 15665–15673, <https://doi.org/10.1021/acs.analchem.4c03129>.
- [18] X.H. Chen, M. Jia, L.H. Liu, X.P. Qiu, H. Zhang, X.L. Yu, W. Gu, G.C. Qing, Q.M. Li, X.L. Hu, R.X. Wang, X.X. Zhao, L.L. Zhang, X.F. Wang, C. Durkan, N. Wang, G. X. Wang, Y. Luo, High-fidelity determination and tracing of small extracellular vesicle cargoes, *SMALL* 16 (40) (2020) 2002800, <https://doi.org/10.1002/smll.202002800>.
- [19] Y.M. Lei, X.C. Fei, Y. Ding, J.H. Zhang, G.H. Zhang, L. Dong, J. Song, Y. Zhuo, W. Xue, P. Zhang, C.Y. Yang, Simultaneous subset tracing and miRNA profiling of tumor-derived exosomes via dual-surface-protein orthogonal barcoding, *Sci. Adv.* 9 (40) (2023) eadi1556, <https://doi.org/10.1126/sciadv.adi1556>.
- [20] D.S. Mao, M.M. Zheng, W.X. Li, Y. Xu, C.G. Wang, Q.L. Qian, S.N. Li, G.F. Chen, X. L. Zhu, X.Q. Mi, Cubic DNA nanocage-based three-dimensional molecular beacon for accurate detection of exosomal miRNAs in confined spaces, *Biosens. Bioelectron.* 204 (2022) 114077, <https://doi.org/10.1016/j.bios.2022.114077>.
- [21] F.Y. Liu, X.M. Liu, W.D. Gao, L.B. Zhao, Q. Huang, T. Arai, Transmembrane capability of DNA origami sheet enhanced by 3D configurational changes, *IScience* 26 (3) (2023) 106208, <https://doi.org/10.1016/j.isci.2023.106208>.
- [22] R. Yan, W. Cui, W. Ma, J. Li, Z. Liu, Y. Lin, Typhaneoside-tetrahedral framework nucleic acids system: mitochondrial recovery and Antioxidation for acute kidney injury treatment, *ACS Nano* 17 (9) (2023) 8767–8781, <https://doi.org/10.1021/acsnano.3c02102>.
- [23] Y. Zhao, S. Li, M. Feng, M. Zhang, Z. Liu, Y. Yao, T. Zhang, Y. Jiang, Y. Lin, X. Cai, Effects of puerarin-loaded tetrahedral framework nucleic acids on osteonecrosis of the femoral head, *Small (Weinheim an der Bergstrasse, Germany)* 19 (41) (2023) e2302326, <https://doi.org/10.1002/smll.202302326>.
- [24] C. Patriarca, P. Colombo, A.P. Taronna, J. Wesseling, G. Franchi, F. Guddo, R. Naspro, R.M. Macchi, P. Giunta, M. Di Pasquale, M. Parente, C. Arizzi, M. Roncalli, B. Campo, Cell Discohesion and Multifocality of carcinoma in situ of the bladder: new insight from the adhesion molecule profile (e-cadherin, ep-CAM, and MUC1), *Int. J. Surg. Pathol.* 17 (2) (2009) 99–106, <https://doi.org/10.1177/1066896908326918>.
- [25] A. Brunner, M. Prelog, I. Verdorfer, A. Tzankov, G. Mikuz, C. Ensinger, EpCAM is predominantly expressed in high grade and advanced stage urothelial carcinoma of the bladder, *J. Clin. Pathol.* 61 (3) (2008) 307–310, <https://doi.org/10.1136/jcp.2007.049460>.